Roughness evolution in strongly interacting donor:acceptor mixtures of molecular semiconductors. An *in situ*, real-time growth study using x-ray reflectivity

G Duva[1,*], L Pithan[2], A Gerlach[1], A Janik[1,4], A Hinderhofer[1] and F Schreiber[1,3]

[1] University of Tübingen, Institute for Applied Physics, Auf der Morgenstelle 10, 72076 Tübingen, Germany
[2] ESRF - The European Synchrotron, 71, Avenue des Martyrs, 38000 Grenoble, France
[3] Center for Light-Matter Interactions, Sensors and Analytics (LISA+), Auf der Morgenstelle 15, 72076 Tübingen, Germany

E-mail: giuliano.duva@uni-tuebingen.de

CrossMark

Abstract

The evolution of surface roughness in binary mixtures of the two molecular organic semiconductors (OSCs) diindenoperylene (DIP) as electron-donor and 1, 3, 4, 5, 7, 8-hexafluoro-tetracyano naphthoquinodimethane (F6TCNNQ) as electron-acceptor is studied. We co-deposit DIP and F6TCNNQ in vacuum with varying relative molar content while keeping a molar excess of DIP in order to produce phase-heterogeneous mixtures. The excess DIP phase segregates in pristine crystallites, whereas the remaining mixed phase is constituted by DIP:F6TCNNQ co-crystallites. We calculate the surface roughness as function of film thickness by modelling x-ray reflectivity data acquired *in situ* and in real-time during film growth. To model the experimental data, two distinct approaches, namely the kinematic approximation and the Parratt formalism, are applied. A comparative study of surface roughness evolution as function of DIP:F6TCNNQ mixing ratio is carried out implementing the Trofimov growth model within the kinematic approximation. Depending on the thickness regime, mixing ratio-specific trends are identified and discussed. To explain them, a growth mechanism for binary heterogeneous mixtures of strongly interacting OSCs is proposed.

S Supplementary material for this article is available online

(Some figures may appear in colour only in the online journal)

1. Introduction

Binary mixtures of molecular organic semiconductors (OSCs), in particular donor:acceptor (D:A) mixtures, represent technologically important systems due to their application as functional layers in optoelectronic devices such as organic field-effect transistors (OFETs), organic light-emitting diodes and in organic photovoltaics [1–4]. The knowledge of surface

roughness during film growth [5] as function of thickness *and* D:A mixing ratio is relevant for devices due to: (a) possible thickness-dependent structural transitions [6–8], (b) the requirement to tune the roughness at the interface between different materials/layers in planar hetero-structures [9], (c) the fact that, in OFETs, the conducting channel extends only in the first few molecular layers of the film [10–12], (d) the dramatic dependence of film optical properties on its thickness and composition [13, 14]. These aspects have to be taken into account during the engineering and optimization process of film thickness and D:A mixing ratio for a given application.

In several studies of molecular thin films of OSCs, x-ray reflectivity (XRR) scans have been measured sequentially in real-time during film growth in order to fit the reflectivity profile at the anti-Bragg point [15–19] as well as at multiple Q_z-points simultaneously [8, 20]. By doing so, quantitative information about the dependence of surface roughness on film thickness can be obtained. However, despite the technological interest of binary systems outlined above, almost all works have focussed on single-component molecular systems. In one work dealing with mixtures of DIP with Buckminster fullerene (C_{60}), the time-evolution of the anti-Bragg oscillations together with the diffuse scattering at low angle have been measured, and from the latter the inter-island distance as function of time has been calculated [21]. There, however, no quantitative evaluation of the film roughness as function of time has been carried out. In another work [22], the roughness evolution of equimolar mixtures of pentacene (PEN) with its per-fluorinated counterpart, perfluoropentacene (PFP), has been calculated by fitting real-time XRR data using the Parratt formalism, but no data fitting employing growth models has been performed. It is thus necessary to quantify the roughness evolution of a broader spectrum of heterogeneous mixtures and correlate it with the molecular structure and mixing behaviour of the constituent materials. Furthermore, such experimental studies can provide precious training data for algorithms based on machine learning, a rapidly expanding field for the prediction of structural and morphological properties of OSCs in the solid state [23–25]. The application of these tools will allow a more rational engineering of functional layers in devices.

The focus of this work is the quantitative modelling of roughness evolution in binary D:A mixtures exhibiting DIP as electron-donating and F6TCNNQ as electron-accepting material. A comparison between two data-analysis approaches is presented and a growth model is proposed. The present work complements our previous studies on this D:A material system exhibiting co-crystal formation as consequence of fairly strong D:A charge-transfer interactions in the ground-state and, at the same time, smooth films in a thickness range of 10–20 nm on native Si oxide for mixtures with DIP excess [26, 27]. The combination of such structural, morphological and optical properties and the possibility to tune them by, e.g., modifying the substrate temperature [28], makes this material system a promising candidate to be employed in functional organic layers for optoelectronic devices.

2. Methods

2.1. Experiment

The molecular OSCs DIP and F6TCNNQ were co-deposited as donor and acceptor materials, respectively, by means of organic molecular beam deposition in a portable vacuum chamber, which allows to carry out *in situ* experiments at synchrotron beamlines [29] (figure 1). In the present work, *in situ* x-ray scattering measurements were carried out at the ID03 beamline (European Synchrotron Research Facility, ESRF) with a beam energy of 24 keV using a Maxipix 2 × 2 detector. We grow mixtures with systematic excess of DIP in order to: (a) obtain films that are smooth enough to be able to follow the evolution of the Kiessig oscillations throughout the entire deposition, (b) identify the first Bragg peak of the excess DIP phase, which would not otherwise be visible in mixtures with equimolar or higher F6TCNNQ content [26].

We measured XRR scans in specular geometry *in situ* and in real-time during the growth of three DIP:F6TCNNQ mixtures with a molar ratio of 6:1, 4:1 and 2:1, respectively, on a Si substrate covered by its native oxide kept at 40°C with a base pressure of $\sim 2 \times 10^{-8}$ mbar. After characterization of a given film, the substrate temperature was raised up to approximately 500°C in vacuum in order to sublimate the organic material, and a fresh spot on the substrate that had not yet been illuminated with the x-rays was used for characterizing the subsequent mixture. The total film thickness and growth rate for the films (DIP:F6TCNNQ mixtures) were 17.5 nm and 0.14 nm/min (6:1), 14.0 nm and 0.14 nm/min (4:1), 17.5 nm and 0.18 nm/min (2:1). For each mixing ratio, the equivalent deposited amount of DIP is calculated using the *total* growth rate measured by means of a quartz-crystal microbalance. The deposition rates were calibrated separately, DIP by means of XRR and F6TCNNQ by means of atomic force microscopy (AFM). With these methods, the error on the mixing ratio is estimated to be ±10%. Measurement of each XRR curve took 150 s, which means that an average of ~ 4 XRR scans are measured for each total deposited monolayer (ML, in units of DIP ML), thus allowing for sub-ML resolution of the growth processes. The data for the mixtures was compared with the data for a pristine DIP film grown in very similar conditions in a previous work [31].

2.2. Growth models and analysis of scattering signal

We fitted the evolution of the XRR scans as function of time using two distinct approaches in order to cross-check the consistency of the results obtained. The first approach consists in fitting the real-time XRR at selected Q_z points simultaneously. The extracted reflectivity profiles exhibit peculiar 'growth oscillations' due to interference caused by the nucleation and gradual filling of new layers. These growth oscillations at fixed Q_z have been fitted by means of the Trofimov growth model [32] built within the kinematic approximation [33]. Note that such an approximation applies well for our
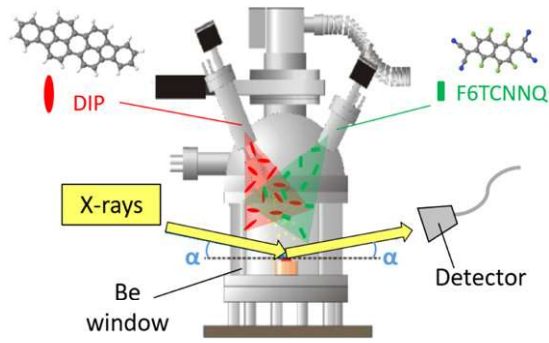
Figure 1. Schematic view of the portable vacuum chamber used in the present work. A cylindrical Be window allows for *in situ* XRR experiments during the co-deposition of DIP and F6TCNNQ. A specular geometry was employed, i.e. the incident and exit angles α are equal. Adapted from reference [30].

system since: (a) the time-profiles have been extracted at Q_z-points well above the critical angle, therefore multiple scattering can be neglected; (b) organic materials are used, therefore the scattering cross section is relatively low and absorption effects can be neglected. In the kinematic approximation, the expression for the reflected intensity as function of time, $I(t)$, can be written as [20]:

$$I(t) = \left| A(Q_z) \cdot e^{i\Phi(Q_z)} + f(Q_z) \sum_n \theta_n(t) \cdot e^{inQ_z d} \right|^2, \quad (1)$$

where $A(Q_z)$ and $\Phi(Q_z)$ are the scattering amplitude and phase from the substrate, respectively, and $f(Q_z)$ is the scattering amplitude from the *single* layers building up the thin film atop. Note that, due to the reflection geometry employed in the present work, only the *z*-component of the total momentum transfer, Q_z, is relevant. The factor $\theta_n(t)$ is the time-dependent layer coverage for the *n*th layer, and the summation runs over all layers *n* which form the film. The three parameters $A(Q_z)$, $\Phi(Q_z)$ and $f(Q_z)$ need to be fitted for each chosen point of the reflectivity curve. The complex exponential factor represents the phase taken upon scattering of the beam from a layer within the thin film, and is modulated by the product $Q_z d$, where $d \equiv d_{DIP}$ is the DIP lattice parameter, which we keep fixed at 16.755 Å. For the special case of the anti-Bragg point, i.e. $Q_z = (1/2) \cdot Q_{Bragg}$, a system of algebraic equations to calculate these three parameters can be obtained [30]. The quantity $\theta_n(t)$ for each layer in equation (1) was obtained by means of the Trofimov growth model [32]. Such model features a system of coupled differential equations, which we write [8, 34]:

$$\frac{d\theta_n}{dt} = R_n(\xi_{n-1} - \theta_n) + R_{n+1}(\theta_n - \xi_n) \quad (2a)$$

$$\xi_n = \begin{cases} 1, & \text{if } n = 0 \\ 0, & \text{if } n \geqslant 1, \ \theta_n < \theta_{cr,n}. \\ 1 - e^{-\left(\sqrt{-\ln(1-\theta_n)} - \sqrt{-\ln(1-\theta_{cr,n})}\right)^2}, & \text{otherwise} \end{cases} \quad (2b)$$

In equation (2a), R_n is the *effective* deposition rate for the *n*th layer and ξ_n describes the formation of a feeding zone (FZ) *on top* of layer *n*, i.e. the fraction of surface on top of the *n*th ML that actually contributes to the growth of the *n*th + 1 ML. The formation and time-evolution of the FZ is described by equation (2b), where the onset for the formation of an FZ is given by the layer-dependent critical layer coverage, $\theta_{cr,n}$. The fitting parameters are, therefore, R_n and $\theta_{cr,n}$. The inclusion of layer-dependent growth rates takes into account the physical observation that the landing molecules might exhibit a layer-dependent sticking coefficient, which seems especially important for molecules landing directly on the bare substrate compared to those landing on an already formed organic layer. Additionally, we impose the condition $\theta_{cr,n} < \theta_{cr,n+1}$ for every *n*. This rests on the assumption that nucleation of any subsequent layer takes place at earlier coverages, a scenario which seems reasonable considering the general tendency of thin films to release thickness-dependent mechanical stresses by accumulating defects, the latter acting as higher-energy centres that promote nucleation. The Trofimov model was implemented and the fits to the data were performed using custom Matlab® scripts. We cross-checked our fits with *Trofit*, a Python implementation of the Trofimov model [35] adapted for fitting multiple Q_z points simultaneously and without imposing $\theta_{cr,n} < \theta_{cr,n+1}$. The differences in terms of residual analysis are not significant and do not affect the comparative study presented further below.

The second approach which we adopted consists in fitting each XRR curve measured during film growth using the Parratt formalism [36, 37], which goes beyond the kinematic approximation and is exact for perfectly flat interfaces. For details on this formalism we refer the reader to references [36, 37]. The Parratt formalism was implemented using the software *Motofit* [38] for the IgorPro package (WaveMetrics Inc.), which makes use of the Abeles matrix formalism for stratified media and assumes the Névot–Croce factor to model interface roughness [33, 37]. The Parratt formalism allows to treat multiple scattering in stratified media. Thus, arbitrary XRR profiles can be fitted and the corresponding electron density as function of film thickness, $\rho_e(z)$, can be obtained. The total coverage of a given *n*th layer was calculated as the ratio between the maximum electron density of the layer itself, $\rho_{e,n}$, and the maximum electron density of the first layer, $\rho_{e,n=1}$, the latter taken for the fully grown film.

Modelling of the layer coverages $\theta_n(t)$ allows to calculate the interface roughness (or root mean-square roughness, σ_{RMS}) as function of time, $\sigma_{RMS}(t)$, using the relationship [34, 39]:

$$\sigma_{RMS}(t) = \sqrt{\sum_{n=1}^{\infty} (\theta_n - \theta_{n+1})(n - C_{tot})^2} \quad (3a)$$

$$C_{tot} = \sum_{n=1}^{\infty} \theta_n. \quad (3b)$$

The quantity C_{tot} in equation (3) is the time-dependent total layer coverage, which, for regular growth with constant rate,

is proportional to the growth time t. The adimensional $\sigma_{RMS}(t)$ obtained with equation (3) is expressed in units of the ML thickness of DIP, d_{DIP}.

Extrapolation of the interface roughness as function of time *and* D:A mixing ratio represents the main result of this work. However, one additional aim of this work is to discuss the advantages and limitations in the use of the above models to describe relatively complicated systems such as D:A mixtures in which co-crystal formation is observed with phase separation of the excess phase, as it is the case for DIP:F6TCNNQ mixed films with excess DIP. We analyse the evolution of surface roughness vs D:A mixing ratio in detail and, supported by complementary structural information (see supporting information, SI (https://stacks.iop.org/JPCM/33/115003/mmedia), we suggest a growth mechanism to explain the observed trends as function of the D:A mixing ratio [22, 40].

3. Results and discussion

The fits carried out with the two approaches outlined in the previous section deliver qualitatively similar results, although quantitative differences emerge. In the following, we first illustrate the results obtained with each model. We then discuss in detail which kind of information each model is best capable of providing. Finally, we use the Trofimov model to guide the interpretation of the roughness evolution as function of DIP:F6TCNNQ mixing ratio.

In figure 2(a), a typical data-set of XRR scans measured *in situ* and in real-time during the growth of the DIP:F6TCNNQ 4:1 mixture is shown. The same kind of data-sets for all DIP:F6TCNNQ mixtures are shown in figure S1 of the SI. The abscissa of the upper plot in figure 2(a) indicates the number of equivalent DIP monolayers deposited, taking into account the DIP:F6TCNNQ molar ratio together with the measured total growth rate. In figure 2(b), the extracted reflectivity-vs-film thickness profiles are plotted against the *total* number of deposited ML according to the thickness monitor. The reflectivity profile at the anti-Bragg point allows to visually follow the filling of each molecular layer [20]. By inspection of the fits, it is possible to see that the Trofimov model is fairly capable of reproducing the experimental trend of the reflectivity-vs-film thickness.

The real-time XRR data presented in figure 2(a) were additionally fitted using the Parratt formalism (figure 3(a)). A multi-layer model was set up in order to reproduce the data in the Q_z-range $\sim$0–0.42 Å^{-1} (see SI, figure S4). To reduce the number of free parameters, we imposed boundary conditions for the electron density, the inter-layer roughness and the monolayer thickness. The fits allow to extract the electron density, ρ_e, as function of z, the depth within the organic film, for each experimental XRR curve (figure 3(b)). The complete sets of Parratt fits of each experimental XRR curve for all three DIP:F6TCNNQ mixtures are reported in figure S5 of the SI.

The average ρ_e has the following values expressed in scattering length density (electron density): 9.50×10^{-6} Å^{-2} (0.337 Å^{-3}) for the 6:1 mixture, 8.85×10^{-6} Å^{-2} (0.314 Å^{-3}) for the 4:1 mixture (figures 3(b)) and 9.55×10^{-6} Å^{-2}

(0.339 Å^{-3}) for the 2:1 mixture. The non-monotonic trend of the average ρ_e as function of mixing ratio seems the result of two competing effects: (a) increasing out-of-plane film disorder with increasing amount of F6TCNNQ, which leads to less compact films and thus lower ρ_e; (b) higher ρ_e of the F6TCNNQ units containing F and N atoms, compared to DIP containing only C and H.

The layer coverages extracted with the Trofimov model and the Parratt formalism for the 4:1 mixture are shown in figure 4(a). As it can be seen, the θ_n extracted with the two different models match fairly well. The curves θ_n for $n = 2$–5 obtained from the Parratt fits saturate slightly above 0.9 instead of 1, which is due to the molecular layer in contact with the substrate having a slightly higher electron density than the upper layers (figure 3(b)). The interface roughness calculated for the 4:1 mixture by means of equation (3) with both models is shown in figure 4(b). Up to a nominal coverage of $\sim$1.5 ML, both models are in good quantitative agreement. Furthermore, up to $\sim$2.5 ML total coverage, the main difference is that the dip in the interface roughness around completion of the 2nd ML is significantly more pronounced in the Trofimov fit than in the Parratt fit, in the latter being only a broad hump. The curves start to deviate substantially starting from $\sim$2.5 ML, with the roughness extracted from the Parratt fits being significantly larger, i.e. more than double the roughness extracted from the Trofimov fits for the largest nominal coverage of 6.5 ML.

3.1. Discussion of fit results

The large discrepancies between the interface roughness obtained from the Trofimov and Parratt models for a total thickness above 2.5 ML (figure 4(b)) can be explained considering two aspects. The first concerns the fact that the Trofimov growth model and the Parratt fits are sensitive to different portions of the XRR profiles. In particular, the Parratt fits include the Q_z region where the Kiessig oscillations appear, therefore they are expected to represent more closely the roughness of the *entire* film. The second aspect is that, for the Parratt fits, the layer coverage saturates slightly above 0.9 for θ_n for $n = 2$–5 (figure 4(a)). Similar results are obtained for the 6:1 and the 2:1 mixtures, although the layer coverages θ_n for $n = 2$–6 of the mixture with highest DIP content does reach saturation (see figure S6 of the SI). Overall, the θ_n extracted from the Parratt fits increase more slowly compared to those extracted from the Trofimov fits (see figure S6 in the SI).

Despite the quantitative differences, we recognize that the results for the interface roughness as function of D:A mixing ratio exhibit the same qualitative trends independent of the data analysis method (compare figure 5(a) to figure S8 of the SI). In the following we consider the number of free parameters *per ML* involved in the two fitting models. As a general approach to our fits, for each model we reduce the number of degrees of freedom *per ML* by imposing boundary conditions. The Trofimov model features three free parameters for the first ML ($n = 1$), namely R_1, R_2 and $\theta_{cr,1}$ (equation (2), see references [32, 39]). We impose $R_{n+1} = R_n$ for $n > 1$, in practice distinguishing only between molecules landing on the bare
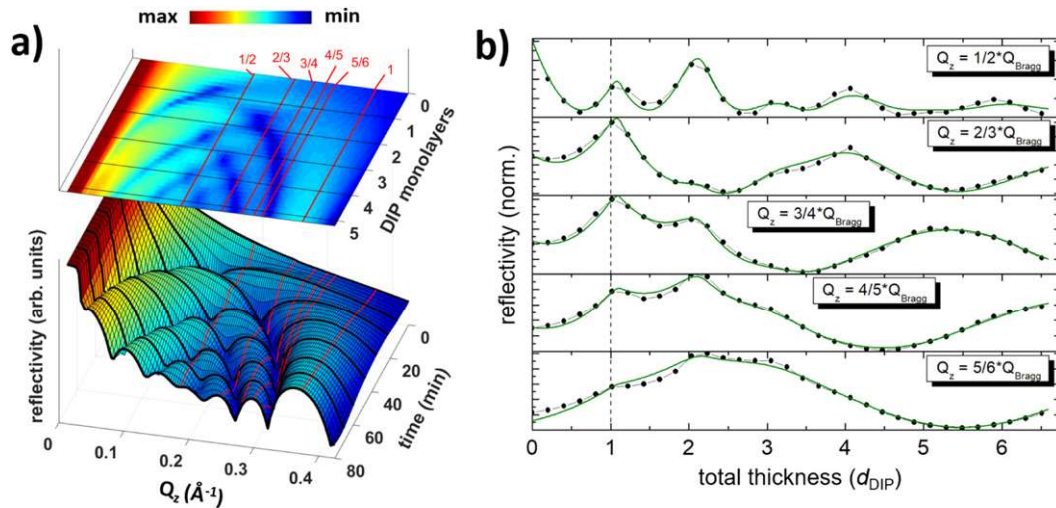
Figure 2. *In situ*, real-time XRR data for the DIP:F6TCNNQ 4:1 mixture. (a) Time evolution of the reflectivity profile. The red lines indicate the fractional points, in units of $Q_{z,\mathrm{Bragg}}$ of the (001)-DIP Bragg peak, at which the time-evolution of the reflectivity has been extracted. A value for $Q_{z,\mathrm{Bragg}} = 0.375$ Å^{-1} is used. The data at time '0 min' corresponds to the first curve measured after exposing the substrate to the molecular flux. The time-cuts highlighted in black are those reported in figure 3(a). The experimental points along Q_z have been interpolated. (b) Extracted profiles at the anti-Bragg point ($Q_z = 1/2 \cdot Q_{\mathrm{Bragg}}$) and other fractions of $Q_{z,\mathrm{Bragg}}$, as indicated in the plots. Fits with the Trofimov model (green) are superimposed to the experimental data. Fits of the monotonically increasing intensity of the Bragg peak ($Q_z = Q_{\mathrm{Bragg}}$) are not shown. The vertical dashed line corresponds to the first total deposited ML (in units of d_{DIP}) as measured with the thickness monitor.
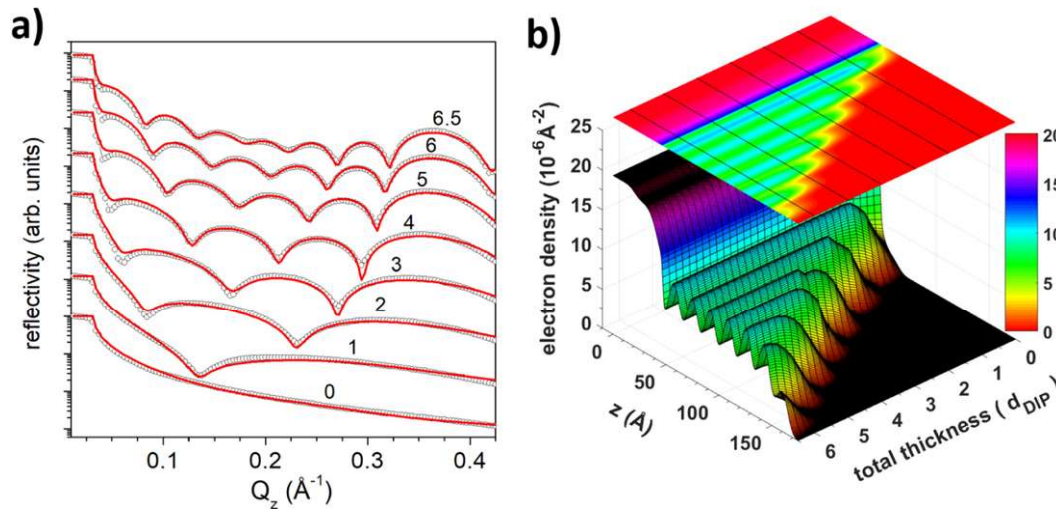

Figure 3. (a) Selected experimental XRR scans (black dotted profiles) and Parratt fits (red profiles) for the DIP:F6TCNNQ 4:1 mixture. The curves were vertically shifted for clarity. Each experimental XRR profile corresponds approximately to the nominal thickness indicated (in units of d_{DIP}). The XRR scans reported here are the same time-cuts highlighted in black in the 3D-plot in figure 2(a). (b) Electron density as function of the z-coordinate perpendicular to the substrate and of the nominal layer coverage expressed as total number of ML deposited (in units of d_{DIP}). Note the colour scale for the electron density.

substrate and on an already formed organic layer [39]. Therefore, already for the second ML ($n = 2$), the only free parameter not coupled to any previously defined parameter is $\theta_{\mathrm{cr},2}$, and this holds for each subsequent ML. The Parratt model features three free parameters per ML, namely the thickness, the electron density and the roughness, but those layers are coupled to each other (for details see figure S4 and the corresponding section in the SI). Although a full statistical analysis evaluating the effect of parameter coupling exceeds the purpose of this

work, overall the differences between the Trofimov and Parratt fits do not seem to depend significantly on the number of free parameters involved.

Next, we consider how the presence of two different phases within a growing film, namely crystalline domains of pristine DIP and D:A co-crystals, has a different impact on the measured reflectivity depending on the Q_z-region considered. In the region of lower Q_z, say, approximately between the total reflection edge and the anti-Bragg point, the Kiessig
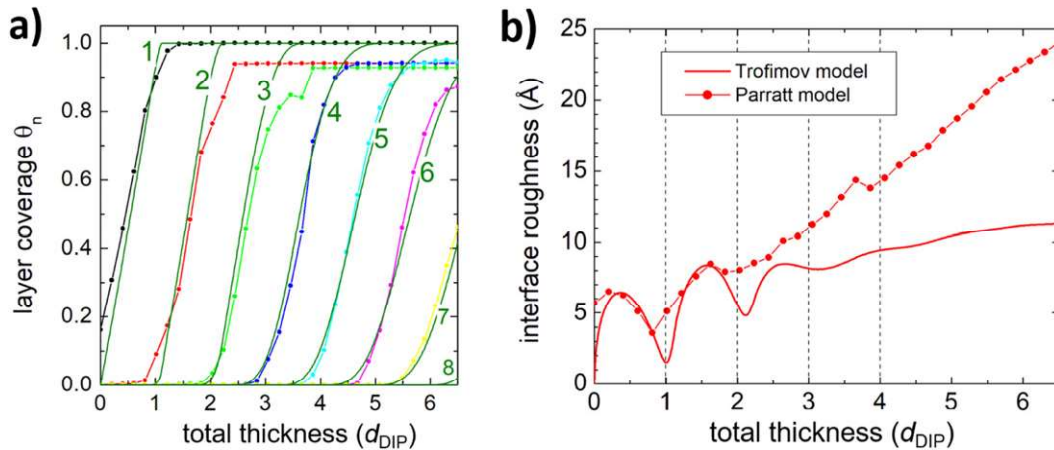
Figure 4. (a) Layer coverage and (b) interface roughness calculated for the DIP:F6TCNNQ 4:1 mixture with the Trofimov and Parratt models. In (a), the curves obtained from the Trofimov fits are full green lines with the layer indexes n indicated, whereas those from the Parratt fits are dotted coloured lines. In (b), the vertical lines correspond to the deposition of the first 4 nominal ML. The nominal film thickness in abscissa is expressed in units of d_{DIP}.
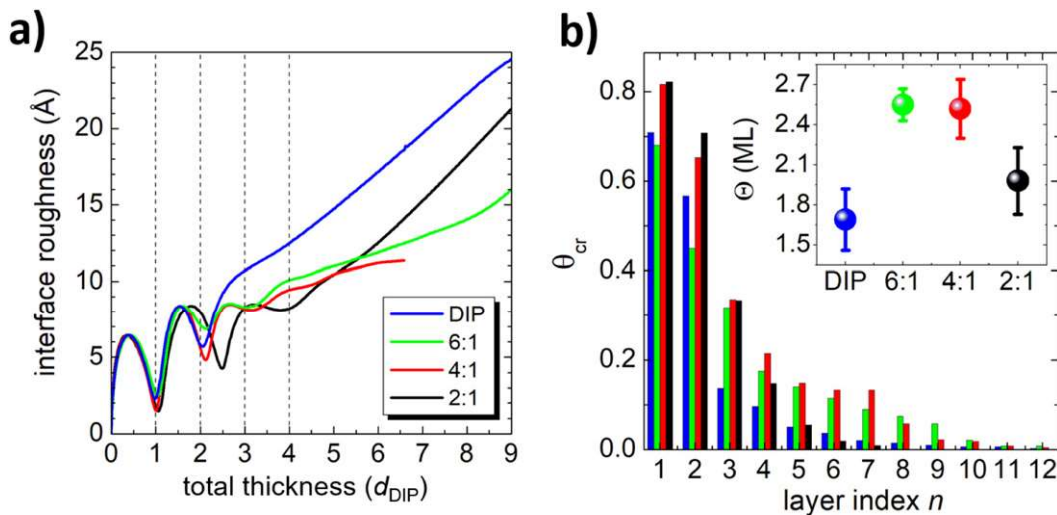
Figure 5. (a) Interface roughness calculated with the Trofimov model as function of nominal film thickness (in units of d_{DIP}). Note that for the 2:1 mixture, due to the relatively high F6TCNNQ content, the actual filling of the 2nd and 3rd layers are delayed significantly compared to the nominal film thickness. (b) Critical layer coverages extracted from the fits (see equation (2b)). The inset shows the parameter Θ extracted from the exponential fits of the critical layer coverages (see main text).

oscillations dominate the reflectivity signal, therefore the data are representative of the laterally averaged reflectivity among the different phases. In the Q_z region between the anti-Bragg point and the first DIP Bragg peak, the shape of the reflectivity is mostly given by the coherent superposition of the scattered waves that gives rise to the Laue oscillations and to the Bragg peak itself [41]. These two types of features depend *only* on crystalline DIP domains in the Q_z region analysed here. Indeed, the first Bragg peak from the D:A co-crystal visible in XRR is located around $Q_z = 0.67$ Å^{-1} and, due to the rather faint out-of-plane coherence of the co-crystallites, does not exhibit Laue side-fringes (see reference [26]). Hence, we assume that the Bragg peak stemming from DIP:F6TCNNQ co-crystallites does not give a sizeable contribution to the reflectivity in this region.

We point out that, at the beginning of the growth, when only ∼1−2 equivalent ML have been deposited on the substrate, there are only ∼1−2 molecular layers stacked on top of each other, hence the vertical coherence, i.e. the strength of the Bragg peak, is rather low. Consequently, interference effects due to crystal coherence and film thickness, respectively, are quite merged, and the Trofimov and Parratt fits give very similar information. This explains the nearly quantitative agreement of the Trofimov and Parratt fits in the thickness range below ∼2.5 ML.

For larger film thickness, the Trofimov fits within the kinematic approximation are more representative of the evolution of the vertical morphology of crystalline DIP domains. However, interference effects between Kiessig oscillations and Laue fringes persist in the whole Q_z-range between the

total reflection edge and the first DIP Bragg peak. In particular, for $Q_z = (1/2) \cdot Q_{z,\text{Bragg}}$ such effects are expected to be most significant, this being the lowest-Q_z point at which the reflectivity-vs-film thickness profiles are extracted. Therefore, the growth oscillations at the anti-Bragg point are also partly affected by the entire film morphology. From all above arguments it follows that the Trofimov fits in the kinematic approximation can help clarifying the growth mechanisms of DIP crystallites while, to some extent, taking into account the entire film morphology. The contribution of the entire film surface morphology to the growth oscillations at fixed Q_z, independently of the material phases formed, is especially relevant in the early growth stages, i.e. in a thickness range up to $\sim$2.5 ML.

The above outlined differences concerning the fitted Q_z-ranges in the two models can explain the quantitative discrepancies of the fits obtained above $\sim$2.5 ML (figure 4(b)). We note that, in order to estimate surface roughness, AFM carried out *ex situ* is often used as a complementary, real-space method to support the analysis of x-ray scattering data in reciprocal space [8, 19, 42]. In the present work we rely on an *in situ* method to follow the growth process in order to exclude possible post-growth effects, such as de-wetting [43]. The following discussion focusses on the different behaviours of interface roughness as function of D:A mixing ratio based on the results from the Trofimov fits. Such model has been widely used to study single-component molecular films [8, 19, 35, 39], hence in the present work we intend to extend its application to the study of binary mixtures.

3.2. Roughness evolution vs D:A mixing ratio

The Trofimov model is used to extract information about the growth mechanisms for the three DIP:F6TCNNQ mixtures studied here. In figure 5, we compare the results for the interface roughness (equation (3)) and critical layer coverage, θ_{cr} (equation (2b)), the latter providing a description of inter-layer transport phenomena. The roughness evolution and extracted θ_{cr} for a pristine DIP film are also shown in figure 5 for comparison. In the following, we first consider the behaviour of the mixtures and then we proceed to make a comparison with pristine DIP.

The 2:1 film exhibits the highest $\theta_{\text{cr},n=1,2}$, which then becomes lower than the 6:1 and 4:1 films for $n \geqslant 3$. We recall that a value of θ_{cr} close to 1 indicates that one layer is nearly completely filled before the next one starts forming on top. Therefore, in a simplified view, having $\theta_{\text{cr}} \approx 1$ corresponds to efficient inter-layer transport, i.e. low Ehrlich–Schwöbel (ES) barrier [44]. This denotes an enhanced layer-by-layer growth character for the first two ML in the 2:1 mixture. For the 3rd ML, the three mixtures exhibit very similar $\theta_{\text{cr},3}$. From the 4th ML on, the 4:1 and 6:1 mixtures exhibit a more pronounced layer-by-layer growth behaviour compared to the 2:1, i.e. $\theta_{\text{cr},n\geqslant 4}$ is smallest for the 2:1 mixture. This trend of $\theta_{\text{cr},n}$ is reflected in the behaviour of the interface roughness which, in the region below a total thickness of $\sim$4 ML, shows dips reaching the lowest roughness values for the 2:1 mixture, thus indicating the highest tendency to fill up a growing layer before

the next one starts forming on top. In this thickness range, the worst layer-filling ability is found for the 6:1 mixture, i.e. the mixture with the highest DIP content, where the dips indicative of a layer-by-layer growth mode are the least pronounced. For all mixtures, the layer-filling efficiency starts to decrease already from the 2nd monolayer, as indicated by the less pronounced dip around 2 ML compared to the dip around 1 ML.

As it can be seen from figure 5(a), the films start roughening significantly from the $\sim$ 5th ML on. The interface roughness values remain below 12 Å for all three mixtures until a total film thickness around 5.5 ML is reached. Within this thickness range, the roughness for the 6:1 mixture exhibits 4 dips, the 4:1 exhibits 5 dips and the 2:1 exhibits 3 dips. For the 6:1 and 4:1 mixtures, the dip at highest total film thickness are almost completely damped out, whereas for the 2:1 mixture the last dip is still quite pronounced. The presence of only three dips for the 2:1 mixture indicates that, for this mixture, layer-filling significantly 'lags' behind the nominal film thickness but is nevertheless effective. These trends indicate that a growth fashion resembling layer-by-layer persists to different extents for all mixtures up to the $\sim$ 5th nominal ML. Interestingly, after extrapolating the roughness of the 4:1 mixture up to a total thickness of 9 ML to allow a comparison with the other mixtures, the 2:1 exhibits the highest roughness. The pronounced layer-by-layer growth fashion exhibited in the earlier growth stages for the 2:1 mixture is, therefore, initially weakened and then 'lost' after a thickness threshold of $\sim$5.5 ML. Overall, the mixing ratio which tends to give the smoothest film is 4:1, i.e. the mixture with intermediate F6TCNNQ content in the range investigated. This reveals an interesting non-monotonic dependence of surface roughness on the DIP:F6TCNNQ mixing ratio in this thickness regime where growth oscillations are fully damped out.

Remarkably, all the mixtures of DIP with F6TCNNQ studied in this work are smoother than pristine DIP grown in very similar conditions (figure 5(a)). For the full dataset and fits for this sample, see figures S2, S7 and S8 of the SI. References [45, 46] contain additional examples of mixing-induced film smoothing in D:A bulk heterojunctions in presence of excess donor species. In those works, however, the molecular species exhibited phase separation due to limited intermixing. The fact that, in our work, the same smoothing effect is observed *also* in mixtures of strongly interacting D:A pairs for which co-crystal formation is observed, might help to shed more light on the fine details of the mechanisms that lead to smoothing.

To further characterize the growth fashion of the films, we carried out a simple exponential fit of the $\theta_{\text{cr},n}$ as function of nominal film thickness for each film (figures S3 and S7 of the SI). The extracted exponential decay factor, $1/\Theta$ (in units of inverse total film thickness), indicates how quick the film tends to roughen (see inset of figure 5(b)). Note that the choice of an exponential to fit the decreasing $\theta_{\text{cr},n}$ is purely functional to the extraction of a figure of merit for film roughening, i.e. another function can in principle be chosen. Inspection of Θ as function of mixing ratio in the inset of figure 5(b) gives a clear indication that a nearly layer-by-layer growth fashion persists

longer for the 6:1 and 4:1 mixtures than for the 2:1, and that the pristine DIP film tends to roughen fastest. However, the parameter Θ for pristine DIP and the mixture with highest content of F6TCNNQ (2:1) are equal within the error bars. This calls out for a more detailed explanation of a complex growth scenario, which we provide in the following section.

4. Growth stages in heterogeneous mixtures

We discuss two possible mechanisms to explain our observations for the molecular system studied here. Importantly, we try to explain the observation that, for the mixtures, the film with the highest F6TCNNQ content exhibits the most pronounced layer-by-layer growth mode in the early growth stages, but the highest roughness in the later growth stages.

We first suggest the following scenario. In the mixed films, F6TCNNQ molecules located at the edges of DIP terraces act as 'defects' [47, 48], lowering the ES barrier for inter-layer diffusion (figure 6) and thereby leading to enhanced layer-by-layer growth [49]. Note that F6TCNNQ molecules might be only 'temporarily' included as defects before a favourable conformation for the nucleation of the DIP:F6TCNNQ co-crystal is found. We note that the lower surface roughness of the mixtures compared to pristine DIP for a total film thickness >2.5 ML (figure 5(a)) agrees in general with a lowering of the ES barrier by admixture of F6TCNNQ. However, although this mechanism explains the observed trend of roughness evolution vs mixing ratio in the low-thickness regime, it does not provide a solid explanation for the trend inversion at larger film thickness. In order to clarify this aspect for the mixed films, one has to take into account the following effects connected with the increasing amount of F6TCNNQ in the mixtures: (a) increase of the relative amount of co-crystal domains compared to pristine DIP, (b) reduction of the coherent size of the pristine DIP crystallites. Both these effects are demonstrated in figure S9 of the SI. We therefore suggest a mechanism that takes into account these observations (figure 7).

We consider the simplest scenario in which D:A co-crystals nucleate only on the bare substrate and not on top of already formed DIP terraces. One has to consider the different rate R_z at which a pristine DIP (R_z^{DIP}) and a DIP:F6TCNNQ co-crystal (R_z^{CC}) grow in the z-direction. We assume here that, during the co-evaporation of DIP and F6TCNNQ, D:A co-crystallites nucleate in the confined spaces between DIP crystallites. This is consistent with the mechanism suggested above for the initial inclusion of F6TCNNQ molecules at step-edges and consequent lowering of the ES barrier. Therefore, in the sub-ML regime, the DIP molecules that land on top of already formed grains or terraces in layer 1 diffuse downwards with high probability due to the presence of F6TCNNQ molecules at the step-edges (figure 6). A fraction of the landing molecules will not diffuse downwards and will thereby contribute to increase the coverage of layer 2. In the Trofimov model, the stage at which this starts is captured by $\theta_{\text{cr},n}$. At this stage, a D:A co-crystal nucleates in the confined interstices between DIP crystallites.

The lateral growth of pristine DIP domains in mixtures with F6TCNNQ is faster than in pristine films due to the
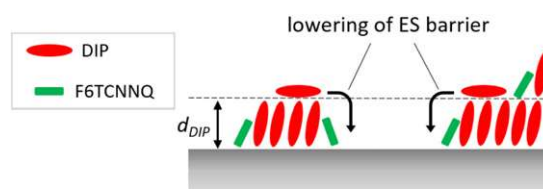
Figure 6. Sketch of the inclusion of F6TCNNQ molecules at the step-edges of pristine DIP crystallites in DIP:F6TCNNQ mixed films, which causes lowering of the ES barrier. The F6TCNNQ molecules act as 'defects' until a suitable conformation for nucleation of the DIP:F6TCNNQ co-crystal is found. The thickness of a DIP ML, d_{DIP}, is shown.
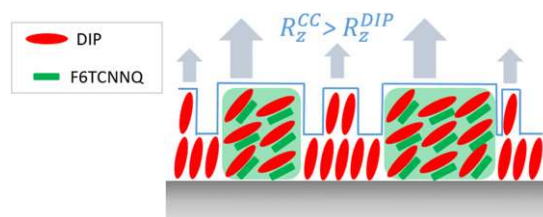
Figure 7. Illustration of the proposed smoothing mechanism during the initial growth stages of D:A mixtures where co-crystal formation is observed. Co-crystal domains are highlighted in green, where the slightly different orientations of the single D:A complexes represent the broader distribution of crystal orientations of the co-crystals compared to DIP crystallites [26]. The blue contour visually defines the film-air interface.

enhancement of inter-layer transport by F6TCNNQ admixing (figure 6). We suggest that the vertical growth of D:A co-crystallites is significantly faster than that of DIP crystallites due to the different surface potential of the heterogeneous crystalline domains, i.e. for the vertical growth rates R_z it holds $R_z^{\text{CC}} > R_z^{\text{DIP}}$. With the assumption that the nucleation of the co-crystal *follows* the nucleation of pristine DIP crystallites in the sub-monolayer regime, the proposed mechanism is consistent with the increasing amount of D:A co-crystals and the concomitant reduction of coherent grain size of DIP as the amount of F6TCNNQ in the mixtures increases (figure S9 of the SI). Additionally, a reduction of the coherent size of DIP crystallites likely leads to a higher density of crystalline defects in DIP domains at later growth stages, which increases the density of nucleation centres for the subsequent layers, leading to a faster lowering of θ_{cr} (figure 5(b)) and thus to enhanced roughening.

The scenario here proposed has some similarities with the 'valley-filling' mechanism proposed to explain smoothing for planar hetero-structures of PFP on DIP and PEN on PFP [31]. However, in our case the filling mechanism works only at low coverages because at some point the vertical growth rate of the co-crystal takes over and causes the film in 2:1 molar ratio to roughen faster than the films with lower F6TCNNQ content. The mechanism we outlined in this work seems to be rather general [49] for 2D-textured, polycrystalline films where two different materials, or the same material but exposing different facets, nucleate and grow in the z-direction with different rates due to a different surface potential of the growing crystallites. Finally, we note that the above picture certainly

represents a simplification of the spectrum of mechanisms at play. Nevertheless it constitutes a starting point to understand the inter-relationships between growth and mixing behaviour of complex, multicomponent molecular systems.

5. Conclusions

In summary, we have carried out a systematic study on bulk heterostructures featuring DIP as donor and F6TCNNQ as acceptor in three different D:A mixing ratios, namely, 6:1, 4:1 and 2:1. This material combination features formation of a D:A co-crystal with phase separation of the excess DIP [26]. The study includes real-time x-ray scattering experiments carried out *in situ* during film growth to elucidate the dependence of film roughness on thickness *and* D:A mixing ratio.

Two approaches of the theory have been compared to extract the interface roughness from the full data-set of time-dependent XRR curves measured for each D:A mixing ratio. The Trofimov growth model, within the framework of the kinematic approximation, and the Parratt formalism have been employed. The sensitivity of each method to different Q_z-ranges of the XRR spectra leads to quantitative differences in the roughness evolution. The quantitative differences are much less pronounced in the early growth stage (total film thickness $\leqslant 2.5$ ML) than in the later stages. This is due to the fact that, in early growth stages, interference effects due to vertical crystal coherence and total film thickness overlap, causing broad fringes in the reflectivity profiles. In general, a similar trend of the roughness as function of film thickness is observed, independently of the model used. This allows us to carry out a comparative study between the three DIP:F6TCNNQ mixing ratios, including pristine DIP as reference, employing the Trofimov model to simultaneously fit the reflectivity along several Q_z points and extract the critical layer coverage $\theta_{cr,n}$, which indicates at which coverage of layer n the layer atop, $n + 1$, nucleates.

Despite the complicated nature of the systems studied here, where phase separation of a D:A crystal is observed aside of the dominant phase of pristine DIP, the combined approaches outlined above allow to draw some general conclusions about the trend of the interface roughness as function of D:A mixing ratio. All mixtures investigated are smoother than pristine DIP above ~ 2.5 ML, which we explain in general with a lowering of the energetic barrier for interlayer transport (ES barrier) due to the presence of F6TCNNQ molecules acting as 'defects' at step edges. Interestingly, the 2:1 mixture exhibits overall the lowest roughness up to a total film thickness ~ 5.5 ML, i.e. the mechanisms that lead to a layer-by-layer growth are most effective for the highest F6TCNNQ content in this thickness regime. However, layer-filling is significantly delayed compared to the nominal film thickness. For the 6:1 mixture with lowest F6TCNNQ content, the layer-by-layer growth is least pronounced. The 4:1 mixture exhibits the highest number of smoothness oscillations up to a total film thickness of ~ 5.5 ML. In a thickness regime above ~ 5.5 ML the 2:1 mixture is the roughest. The obtained trends show that the 2:1 mixture exhibits the largest relative changes in roughness going

from the earlier growth stages to the later ones. This behaviour has been tentatively explained with a mechanism that considers two relevant phenomena that occur for increasing amounts of F6TCNNQ, namely, lowering of the ES barrier and formation of D:A co-crystals. On the one side, the vertical growth rate of D:A co-crystallites, R_z^{CC}, overtakes the vertical growth rate of pristine DIP crystallites, R_z^{DIP}, after a total film thickness of ~ 5.5 ML. On the other side, the increasing relative amount of F6TCNNQ leads to a higher defect density in pristine DIP domains. Both these phenomena lead to the mixing ratio-dependent roughness evolution.

This study is of fundamental interest for device architectures. Indeed, it is a common observation that for thin films of OSCs several phenomena exhibit a dependence on film thickness, like the occurrence of a different crystal polymorph or the onset of film roughening. We therefore recommend to extend our methodology to further mixed molecular systems of technological relevance, in particular by performing comparative studies among different mixing ratios.

ORCID iDs

G Duva https://orcid.org/0000-0001-9492-3276
A Gerlach https://orcid.org/0000-0003-1787-1868
F Schreiber https://orcid.org/0000-0003-3659-6718

References

[1] Forrest S R 1997 *Chem. Rev.* **97** 1793
[2] Walzer K, Maennig B, Pfeiffer M and Leo K 2007 *Chem. Rev.* **107** 1233
[3] Opitz A, Wagner J, Brütting W, Salzmann I, Koch N, Manara J, Pflaum J, Hinderhofer A and Schreiber F 2010 *IEEE J. Sel. Top. Quantum Electron.* **16** 1707
[4] Lüssem B, Tietze M L, Kleemann H, Hoßbach C, Bartha J W, Zakhidov A and Leo K 2013 *Nat. Commun.* **4** 2775
[5] Krug J 1997 *Adv. Phys.* **46** 139
[6] Dürr A C, Schreiber F, Ritley K A, Kruppa V, Krug J, Dosch H and Struth B 2003 *Phys. Rev. Lett.* **90** 016104
[7] Kowarik S, Gerlach A, Sellner S, Schreiber F, Cavalcanti L and Konovalov O 2006 *Phys. Rev. Lett.* **96** 125504
[8] Sparenberg M *et al* 2014 *Phys. Chem. Chem. Phys.* **16** 26084
[9] Hinderhofer A and Schreiber F 2012 *Chem. Phys. Chem.* **13** 628
[10] Dodabalapur A, Torsi L and Katz H E 1995 *Science* **268** 270
[11] Dinelli F, Murgia M, Levy P, Cavallini M, Biscarini F and de Leeuw D M 2004 *Phys. Rev. Lett.* **92** 116802

[12] Liscio F *et al* 2013 *ACS Nano* **7** 1257
[13] Heinemeyer U, Broch K, Hinderhofer A, Kytka M, Scholz R, Gerlach A and Schreiber F 2010 *Phys. Rev. Lett.* **104** 257401
[14] Broch K, Gerlach A, Lorch C, Dieterle J, Novák J, Hinderhofer A and Schreiber F 2013 *J. Chem. Phys.* **139** 174709
[15] Krause B, Schreiber F, Dosch H, Pimpinelli A and Seeck O H 2004 *Europhys. Lett.* **65** 372
[16] Desai T V, Woll A R, Schreiber F and Engstrom J R 2010 *J. Phys. Chem. C* **114** 20120
[17] Desai T V, Hong S, Woll A R, Hughes K J, Kaushik A P, Clancy P and Engstrom J R 2011 *J. Chem. Phys.* **134** 224702
[18] Desai T V, Kish E R, Woll A R and Engstrom J R 2011 *J. Phys. Chem. C* **115** 18221
[19] Frank C, Novák J, Banerjee R, Gerlach A, Schreiber F, Vorobiev A and Kowarik S 2014 *Phys. Rev. B* **90** 045410
[20] Kowarik S, Gerlach A, Skoda M W A, Sellner S and Schreiber F 2009 *Eur. Phys. J. Spec. Top.* **167** 11
[21] Lorch C *et al* 2017 *J. Chem. Phys.* **146** 052807
[22] Hinderhofer A, Frank C, Hosokai T, Resta A, Gerlach A and Schreiber F 2011 *J. Chem. Phys.* **134** 104702
[23] Gryn'ova G, Lin K-H and Corminboeuf C 2018 *J. Am. Chem. Soc.* **140** 16370
[24] Musil F, De S, Yang J, Campbell J E, Day G M and Ceriotti M 2018 *Chem. Sci.* **9** 1289
[25] Greco A, Starostin V, Karapanagiotis C, Hinderhofer A, Gerlach A, Pithan L, Liehr S, Schreiber F and Kowarik S 2019 *J. Appl. Crystallogr.* **52** 1342
[26] Duva G *et al* 2018 *J. Phys. Chem. C* **122** 18705
[27] Duva G, Beyer P, Scholz R, Belova V, Opitz A, Hinderhofer A, Gerlach A and Schreiber F 2019 *Phys. Chem. Chem. Phys.* **21** 17190
[28] Duva G, Mann A, Pithan L, Beyer P, Hagenlocher J, Gerlach A, Hinderhofer A and Schreiber F 2019 *J. Phys. Chem. Lett.* **10** 1031
[29] Ritley K A, Krause B, Schreiber F and Dosch H 2001 *Rev. Sci. Instrum.* **72** 1453
[30] Kowarik S 2006 Real-time studies of thin film growth of organic semiconductors *PhD Thesis* Wadham College, Oxford
[31] Hinderhofer A, Gerlach A, Kowarik S, Zontone F, Krug J and Schreiber F 2010 *Europhys. Lett.* **91** 56002
[32] Trofimov V I and Mokerov V G 2003 *Thin Solid Films* **428** 66
[33] Als-Nielsen J and McMorrow D 2011 *Elements of Modern X-Ray Physics* 2nd edn (New York: Wiley)
[34] Pithan L 2017 On the role of external stimuli to tailor growth of organic thin films *PhD Thesis* Humboldt Universität, Berlin
[35] Beyer P *et al* 2014 *ACS Appl. Mater. Interfaces* **6** 21484
[36] Parratt L G 1954 *Phys. Rev.* **95** 359
[37] Tolan M 1999 *X-Ray Scattering from Soft-Matter Thin Films: Materials Science and Basic Research* (*(Springer Tracts in Modern Physics)*) (Berlin: Springer)
[38] Nelson A 2006 *J. Appl. Crystallogr.* **39** 273
[39] Woll A R, Desai T V and Engstrom J R 2011 *Phys. Rev. B* **84** 075479
[40] Reinhardt J P, Hinderhofer A, Broch K, Heinemeyer U, Kowarik S, Vorobiev A, Gerlach A and Schreiber F 2012 *J. Phys. Chem. C* **116** 10917
[41] Dürr A C, Schreiber F, Münch M, Karl N, Krause B, Kruppa V and Dosch H 2002 *Appl. Phys. Lett.* **81** 2276
[42] Zhang X, Barrena E, Goswami D, de Oteyza D G, Weis C and Dosch H 2009 *Phys. Rev. Lett.* **103** 136101
[43] Kowarik S, Gerlach A, Sellner S, Cavalcanti L and Schreiber F 2009 *Adv. Eng. Mater.* **11** 291
[44] Bommel S *et al* 2014 *Nat. Commun.* **5** 5388
[45] Banerjee R, Novák J, Frank C, Lorch C, Hinderhofer A, Gerlach A and Schreiber F 2013 *Phys. Rev. Lett.* **110** 185506
[46] Lorch C, Broch K, Belova V, Duva G, Hinderhofer A, Gerlach A, Jankowski M and Schreiber F 2016 *J. Appl. Crystallogr.* **49** 1266
[47] Koller G, Surnev S, Ramsey M G and Netzer F P 2004 *Surf. Sci.* **559** L187
[48] Hlawacek G, Puschnig P, Frank P, Winkler A, Ambrosch-Draxl C and Teichert C 2008 *Science* **321** 108
[49] Hinderhofer A *et al Phys. Rev. Lett.* (in review)